

# Engineering nanoscale hypersonic phonon transport

**Omar Florez**

Catalan Institute of Nanoscience and Nanotechnology (ICN2), CSIC and BIST, Campus UAB,

**Guillermo Arregui**

Department of Photonics Engineering, DTU Fotonik, Technical University of Denmark, Building 343, DK-2800

**Marcus Albrechtsen**

Technical University of Denmark <https://orcid.org/0000-0003-4226-0997>

**Ryan Ng**

Catalan Institute of Nanoscience and Nanotechnology (ICN2), CSIC and BIST, Campus UAB,

**Jordi Gomis-Bresco**

Departament de Física Aplicada, Universitat de Barcelona, IN2UB, 08028

**Søren Stobbe**

Technical University of Denmark <https://orcid.org/0000-0002-0991-041X>

**Clivia Sotomayor Torres**

ICN2 - Catalan Institute of Nanoscience and Nanotechnology <https://orcid.org/0000-0001-9986-2716>

**Pedro David García** (✉ [pd.garcia@csic.es](mailto:pd.garcia@csic.es))

Instituto de Ciencia de Materiales de Madrid (ICMM), Consejo Superior de Investigaciones Científicas (CSIC) <https://orcid.org/0000-0002-3422-178X>

---

## Research Article

### Keywords:

**Posted Date:** February 18th, 2022

**DOI:** <https://doi.org/10.21203/rs.3.rs-1342422/v1>

**License:**  This work is licensed under a Creative Commons Attribution 4.0 International License.

[Read Full License](#)

---

**Version of Record:** A version of this preprint was published at Nature Nanotechnology on August 8th, 2022. See the published version at <https://doi.org/10.1038/s41565-022-01178-1>.

# Engineering nanoscale hypersonic phonon transport

O. Florez,<sup>1,2,\*</sup> G. Arregui,<sup>1</sup> M. Albrechtsen,<sup>3</sup> R. C. Ng,<sup>1</sup> J. Gomis-Bresco,<sup>1</sup>  
S. Stobbe,<sup>3,4</sup> C. M. Sotomayor-Torres,<sup>1,5</sup> and P. D. García<sup>1,†</sup>

<sup>1</sup>*Catalan Institute of Nanoscience and Nanotechnology (ICN2),  
CSIC and BIST, Campus UAB, Bellaterra, 08193 Barcelona, Spain*

<sup>2</sup>*Dept. de Física, Universitat Autònoma de Barcelona, 08193 Bellaterra, Spain*

<sup>3</sup>*Department of Photonics Engineering, DTU Fotonik,  
Technical University of Denmark, Building 343, DK-2800 Kgs. Lyngby, Denmark*

<sup>4</sup>*NanoPhoton - Center for Nanophotonics, Technical University of Denmark,  
Ørsteds Plads 345A, DK-2800 Kgs. Lyngby, Denmark*

<sup>5</sup>*ICREA - Institució Catalana de Recerca i Estudis Avançats, 08010 Barcelona, Spain*

(Dated: February 9, 2022)

Controlling the vibrations in solids is crucial to tailor their mechanical properties and their interaction with light. Thermal vibrations represent a source of noise and dephasing for many physical processes at the quantum level. One strategy to avoid these vibrations is to structure a solid such that it possesses a phononic stop band, i.e., a frequency range over which there are no available mechanical modes. Here, we demonstrate the complete absence of mechanical vibrations at room temperature over a broad spectral window, with a 5.3 GHz wide band gap centered at 8.4 GHz in a patterned silicon nanostructure membrane measured using Brillouin light scattering spectroscopy. By constructing a line-defect waveguide, we directly measure GHz localized modes at room temperature. Our experimental results of thermally excited guided mechanical modes at GHz frequencies provides an efficient platform for photon-phonon integration with applications in optomechanics and signal processing transduction.

Nanostructured materials offer the possibility to manipulate the mechanical vibrations of a solid over a specified spectral bandwidth. This in turn enables the control of light-matter interactions in the visible and near-infrared regimes for optomechanical applications ranging from high-resolution accelerometers [1] to mass and force sensors [2, 3], in addition to providing fundamental insight into phenomena such as quantum ground-state cooling [4, 5]. By periodically distributing the mass within a system, it is possible to engineer its mechanical modes [6, 7] and open frequency windows over which the destructive interference of scattered waves forbids any phonon propagation [8, 9]. This approach enables engineering of the thermal conductance of the structure [10] and allows for the routing of phonons at the mesoscale [11, 12]. Although full-gap GHz phononic crystals are widely used in optomechanical systems to create phononic shields [13], waveguides [14, 15], and cavities [16, 17], clear and direct experimental evidence of a complete omnidirectional phononic band gap at hypersonic (GHz) frequencies is still lacking. Existing experimental work is generally limited to MHz frequencies, using piezoelectric materials to drive the system [18–20], requiring varying interdigitated electrodes to probe different frequencies and propagation directions. In the GHz regime, only partial and narrow mechanical band gaps (with up to 8% gap to mid-gap ratio) have been shown using assembled platforms such as colloidal crystals [21] or two-dimensional phononic crystal membranes [22]. Furthermore, the control and guiding of mechanical waves at GHz frequencies has been difficult to achieve or measure, relying on complex optomechanical systems [14, 15], or nonlinear stimulated phenomena [23].

Here, we report direct experimental evidence of a wide full phononic gap with a central frequency at 8.4 GHz and a spectral width of 5.3 GHz (a gap to mid-gap ratio of 64%) in a free-standing patterned silicon membrane phononic crystal. Additionally, we create a line-defect waveguide with the same geometry in which we directly measure two guided modes at 5.7 and 7.1 GHz within the band gap at room temperature. We demonstrate the spectral tunability of the mechanical gap from approximately 4 to 12 GHz, which subsequently enables spec-

tral tunability of the guided modes. All the structures measured here are fabricated on a silicon-on-insulator (SOI) platform, which readily enables integration with electronic and photonic circuits. Figure 1(a) shows a scanning electron micrograph (SEM) of the fabricated pattern composed of a triangular array of “shamrocks” [24, 25], formed by three tangential circles with nominal parameters of thickness  $t = 220$  nm, period  $a = 330$  nm, and radius  $r = 0.22a$ , as detailed in the inset of Fig. 1(a) and Fig. S1 in the supplementary information (SI). We calculate the mechanical dispersion relation of the structure by solving the full three-dimensional elastic wave equation using finite-element (FEM) simulations performed with COMSOL Multiphysics [26]. Figure 1(b) plots the symmetric (blue) and asymmetric (red) acoustic modes with respect to the mid-plane of the silicon slab, calculated over the entire first Brillouin zone (BZ) of the crystal. We use the geometrical parameters extracted from SEM images to more accurately simulate the real shape of the fabricated crystal (see Fig. S3 in SI for a statistical analysis). We also take into account the anisotropy of the silicon stiffness tensor and its particular orientation with respect to the fabricated samples, as detailed in Fig. 1(a). Due to this mechanical anisotropy, the irreducible BZ is determined by the first quarter of the hexagon highlighted on the bottom part of Fig. 1(b) (see section S3 in SI). A full mechanical gap opens between the 6th and 7th bands, from 6.7 GHz up to 11.4 GHz (gap to mid-gap ratio of 52 %) which results in the complete depletion of the phonon density of states (DOS) over this frequency range, as shown in Fig. 1(c). The particular shape of the shamrock crystal, which is comprised of large masses connected by small necks, enables a distribution of the mass within the unit cell that results in this broad mechanical gap. A direct link exists between the spectral width of the gap and the narrow necks (shorter distance between shamrocks): a larger radius leads to narrower connected neck regions, which subsequently widens the gap [27].

We use Brillouin light-scattering spectroscopy [28, 29] to reconstruct the mechanical dispersion relation of the system. For simplicity, we probe the band structure along the  $\Gamma K M \Gamma$  path, highlighted at the bottom of Fig. 1(b), as the edges of the gap do not change in frequency with respect to the irreducible BZ (see section S2 in SI). When incident light with frequency  $\nu_i$  and wavevector  $\vec{k}_i$  reaches the surface of the sample with a certain angle,  $\theta$ , as illustrated in Fig. 2(a), part of it is linearly scattered while another small part is nonlinearly scattered in all directions by thermally activated acoustic phonons. This scattering process occurs either by the elasto-optic [30] or the

\*Electronic address: omar.florez@icn2.cat

†Electronic address: pd.garcia@csic.es; current address: Instituto de Ciencia de Materiales de Madrid (ICMM), Consejo Superior de Investigaciones Científicas (CSIC), Calle Sor Juana Inés de la Cruz, 3, 28049 Madrid, Spain.

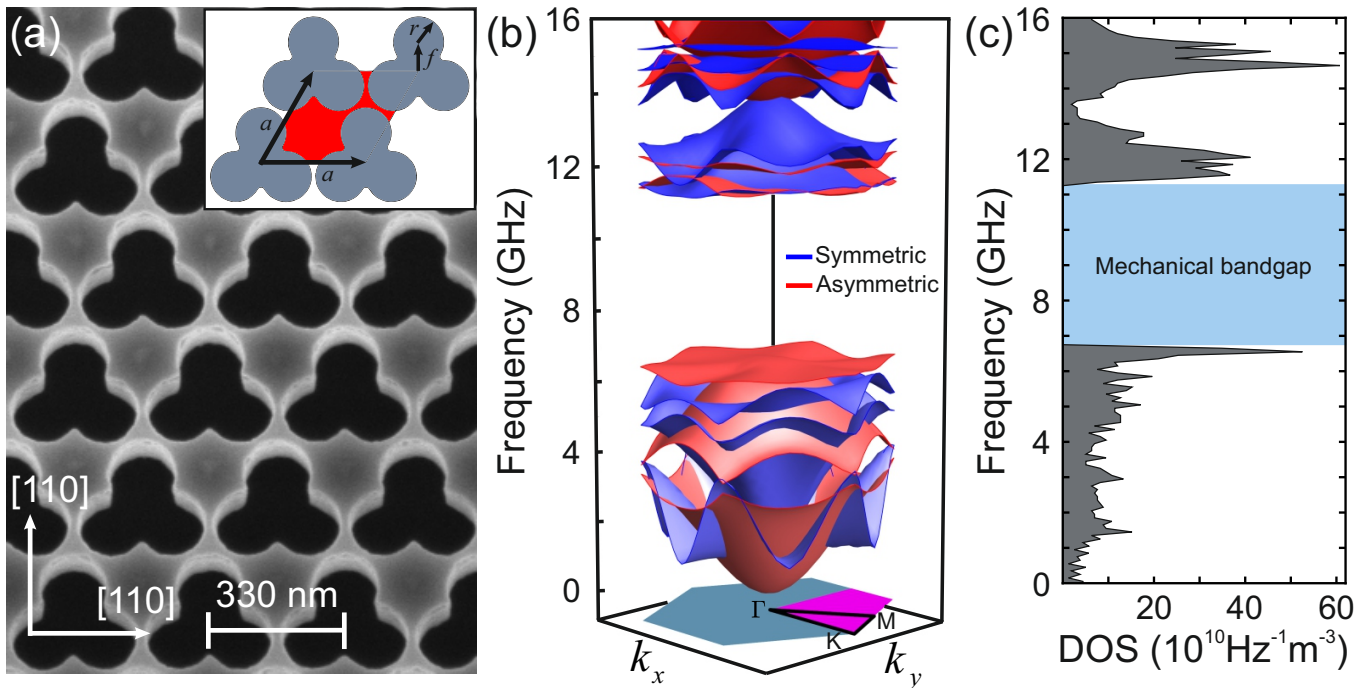


**Figure 1: Shamrock phononic insulator.** (a) Scanning-electron micrograph (tilted-top view) of the fabricated structure on a silicon-on-insulator substrate with a thickness of  $t = 220$  nm. The inset schematically illustrates the geometrical parameters of the unit cell (highlighted in red) with lattice constant  $a = 330$  nm, hole radius  $r = 0.22a$ , and the distance between the center of the shamrock and the center of each circle  $f = 2r/\sqrt{3}$ . (b) Simulated 3D mechanical dispersion relation of the crystal over the first Brillouin zone. Blue and red curves indicate the symmetric and asymmetric modes with respect to the middle plane of the silicon slab at  $t/2$ . (c) Calculated phononic density of states (DOS) of the structure. The light-blue region highlights the full mechanical gap spanning 6.7 GHz to 11.4 GHz.

moving-boundary (MB) [31] mechanism. The former is a volumetric effect caused by the acoustic modulation of the dielectric constant  $\epsilon$  inside the material, while the latter is a surface effect induced by the movement of phonons that creates corrugation at the interface. The interplay between these two effects can result in the enhancement [32] or the cancellation [33] of the scattering process. Given the high refractive-index contrast between silicon and the surrounding air, and the small volume of interaction, determined by the direction of the incident beam and the thickness of the suspended structure, the scattering process here is dominated by the MB mechanism (see S4 in the SI). Our experiment collects the backscattered signal,  $\vec{k}_s$ . For this configuration, the phase-matching condition for the mechanical wavevector  $\vec{q}_{\parallel}$ , which lies parallel to the surface, is determined by

$$q_{\parallel} = 2k_i \sin \theta = \frac{4\pi}{\lambda_i} \sin \theta, \quad (1)$$

where  $k_i = 2\pi/\lambda_i$ . Therefore, it is possible to probe different mechanical wavevectors by changing the angle of incidence of light  $\theta$ , illustrated in Fig. 2(a), and subsequently map the dispersion relation of the acoustic phonons. All measurements were taken by focusing a green laser ( $\lambda_i = 532$  nm) that is  $p$ -polarized with respect to the sagittal plane formed by the angle  $\theta$  (see Fig. S6 in SI). The scattered light that was analyzed is also the  $p$ -polarized component. Although in-plane and out-of-plane mechanical modes in bulk materials and membranes can be selectively detected using light polarization [34], mechanical modes in phononic crystals are generally mixed. Therefore, we do not obtain different information by considering different polarizations of incident and analyzed light. Figure 2(b) plots the mechanical spectrum measured with incident angle  $\theta = 32.5^\circ$ , which corresponds to the high-symmetry point  $K$  in reciprocal space. The central peak highlighted in green corresponds to the elastic (Rayleigh) scattered signal. Positive and negative frequencies correspond with anti-Stokes and Stokes contributions respectively, which are equally likely in a stochastic process such as spontaneous Brillouin scattering [30, 35]. All

the peaks observed in the spectrum correspond to vibrational modes of the system and their amplitudes depend on the scattering efficiency of each mode with the incident laser light [36], which is proportional to the displacement of the boundaries, as previously mentioned and detailed in section S4 of the SI. We obtain the phonon frequencies by fitting each of the observed peaks to Lorentzian line shapes and extracting the mean value between the resonant frequencies of the Stokes and anti-Stokes components. Figure 2(c) plots the mechanical dispersion relation along the  $\Gamma K M \Gamma$  path. The intensity color scale represents the normalized coupling coefficients for the MB perturbation.

The sidewalls of our structures are angled at  $4^\circ$  relative to vertical, which is taken into account in our band structure calculation, as shown in the inset of Fig. 2(c). This breaks the up-down symmetry and the mechanical modes of the real structure therefore can not be classified by their symmetry with respect to the mid plane of the slab as done previously in Fig. 1(b). For this reason, all bands in Fig. 2(c) are indicated with the same color and only change in intensity to indicate the scattering efficiency of each mode and wavevector. We observe that this small correction to the vertical profile causes a displacement of about 1 GHz in the bands below the band gap which becomes evident upon comparing Fig. 2(c) and Fig. 1(c). Additionally, the gap to mid-gap ratio increases from 52 % in Fig. 1(b) and 1(c), to 64 % in Fig. 2(c). The black dots in Fig. 2(c) are the measured frequencies of the peaks as the incident angle is varied. The vertical dotted line indicates the position of frequencies obtained for the spectrum shown in Fig. 2(b).

To resolve the full mechanical dispersion relation, we map the highest-symmetry directions of the Brillouin zone:  $\Gamma K$ ,  $KM$ , and  $\Gamma M$ . The  $\Gamma K$  path is measured by varying the angle of incidence  $\theta$  from zero to  $32.5^\circ$ , as depicted in Fig. 2(d) where the green arrow represents the incident laser. Here, the value of the maximum angle  $\theta$  is calculated from the relation  $|\Gamma K| = \frac{4\pi}{3a} = \frac{4\pi}{\lambda_i} \sin \theta$ . To map the  $\Gamma M$  direction, we rotate the sample 30 degrees to align the  $\Gamma M$  path with the horizontal direction as indicated in Fig. 2(f) and, from that position, we

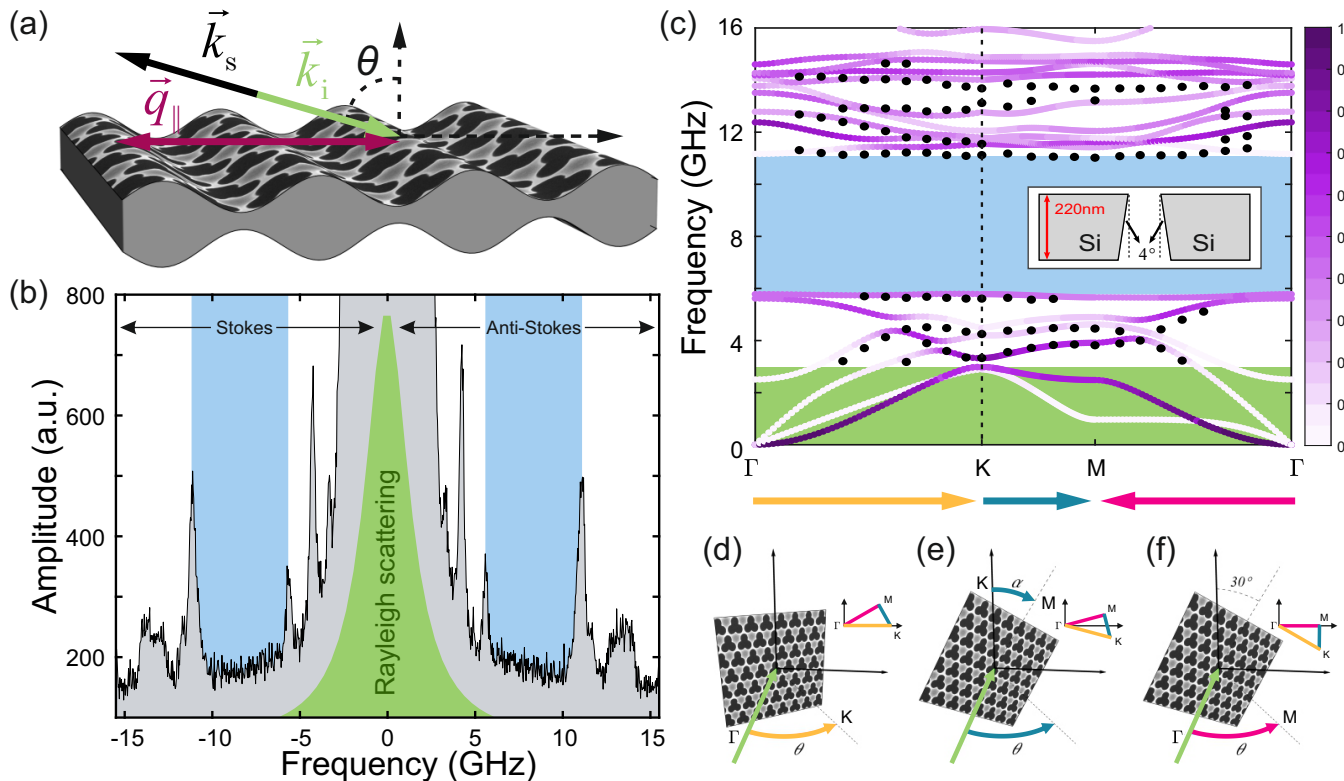


**Figure 2: Brillouin light scattering spectroscopy.** (a) Schematic illustration of Brillouin scattering with the phase-matching condition for the backward configuration used in the experiments. Here,  $\vec{k}_i$  and  $\vec{k}_s$  represent the incident and the scattered light, respectively, and  $\vec{q}_{\parallel}$  is the parallel mechanical wavevector. The magnitude of  $\vec{q}_{\parallel}$  depends on the incident angle, where  $q_{\parallel} = 2k_i \sin \theta$ . (b) Measured Brillouin scattering spectrum for an incident angle of  $\theta = 32.5^\circ$  with  $p$ -polarized light. The green central peak stems from elastic Rayleigh scattering. Negative and positive frequency peaks on either side of this large central peak correspond to Stokes and anti-Stokes contributions, respectively. The light-blue regions highlight the mechanical gap. (c) Calculated dispersion relation based on the geometrical parameters obtained from SEM images of the fabricated samples that include a  $4^\circ$  sidewall angle correction in the vertical profile (inset). The black dots represent the measured frequencies of vibrational modes for different angles and the vertical dotted line indicates the frequencies obtained from the measured spectrum shown in (b). The intensity color scale represents the normalized coupling coefficients for the MB perturbation. (d), (e) and (f) indicate the direction in which the sample is physically rotated to scan along the highest-symmetry directions  $\Gamma K$ ,  $KM$ , and  $\Gamma M$ , respectively. The green arrows indicate the direction of the incident laser light while the other colored arrows correspond to the rotation direction during measurements, which represent (and are color-consistent with) the highest-symmetry direction indicated in (c).

rotate the angle  $\theta$ . Here, the maximum angle is indicated by  $|\Gamma M| = \frac{2\pi}{\sqrt{3}a} = \frac{4\pi}{\lambda_i} \sin \theta$ . Mapping the  $KM$  path requires the simultaneous variation of two specific angles  $\alpha$  and  $\theta$  to measure the intersecting point of the blue segment and the horizontal direction, as depicted in Fig. 2(e). The calculated and measured frequencies are in good agreement and we attribute the residual frequency mismatch to fabrication fluctuations and the non-vertical sidewalls. Some modes in Fig. 2(c) are undetectable in the experiment as their displacement is predominantly in-plane and therefore do not scatter enough light to be detected. The light-blue region in Fig. 2(c) highlights the mechanical gap of this particular crystal. Within this frequency window, no mechanical modes were measured for any angle of incidence in any high-symmetry direction, covering a broad spectral range of 5.3 GHz centered at 8.4 GHz, which corresponds to a gap to mid-gap ratio of 64%. This crystal has the largest measured mechanical gap in the hypersonic regime to date. We also explore the possibility to spectrally tune the gap as a function of the geometry by variation of the lattice constant  $a$ . The band gap evolution calculated from FEM and measured spectra for crystals with periods of 220 nm, 330 nm and 440 nm, can be found in section S5 of SI. We confirm the spectral tunability of the gap from 4 to 12 GHz. Subsequently, tuning of phononic guided modes is also possible.

Finally, we demonstrate the possibility to create phononic waveguides with the phononic insulator presented here. For this, we design and fabricate a waveguide surrounded on both sides by shamrock phononic crystals with inverted symmetry

as shown in the SEM image in Fig. 3(a). This structure has a periodicity of  $a = 440$  nm, a waveguide width of  $w = 184$  nm, and the same fill fraction and thickness as the previous structures ( $r/a = 0.22$ ,  $t = 220$  nm). The mirror symmetry of the crystal with respect to the defect line is crucial for proper band engineering of the guided mechanical modes. The two panels in Fig. 3(b) show the Brillouin spectra measured on the waveguide (top), and on the surrounding phononic crystal (bottom), as specified in the insets, taken at the same incident angle of  $23.8^\circ$ . The blue region indicates the phononic band gap of the structure. The two peaks measured within this gap in the top panel of Fig. 3(b) at 5.7 GHz and 7.1 GHz are clear experimental evidence of mechanical vibrations localized in the phononic waveguide. In order to detect these localized modes, it is necessary to focus the light on the waveguide with a long-working distance microscope objective to reduce the spot size of the incident light down to  $1.2 \mu\text{m}$ . In doing so, we reduce the contribution of the Brillouin scattered signal from the crystal while increasing the contribution from the waveguide. For the measurements of these waveguide structures, the background is higher due to a greater collection of reflected and linearly scattered light relative to that of the 3 cm lens used in Fig. 2. Figure 3(c) plots the dispersion relation of the waveguide accounting for the  $4^\circ$  correction of the vertical sidewalls. As in Fig. 2c, the color intensity of the bands corresponds to the normalized coupling coefficient for the MB perturbation. The fully shaded regions above and below the gap correspond to the bulk crystal modes and define the band gap edges of the structure. The

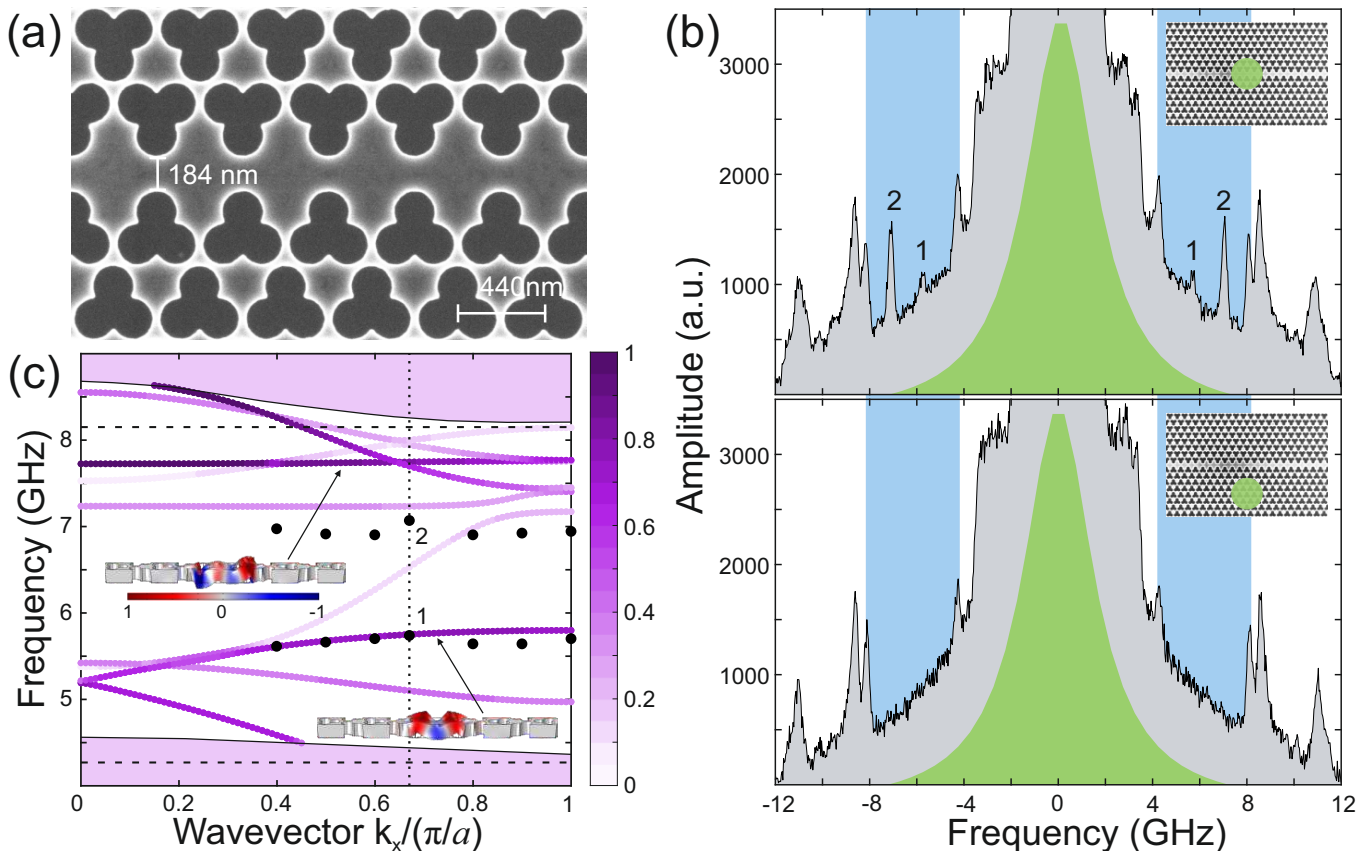


**Figure 3: Hypersonic phononic waveguide** (a) SEM image of a shamrock phononic waveguide with a lattice period of  $a = 440$  nm and waveguide width of  $w = 184$  nm. The thickness and radius of the structure are the same as in previous structures ( $t = 220$  nm,  $r = 0.22a$ ). (b) Measured Brillouin scattering spectra in the waveguide (top) and surrounding phononic crystal (bottom) as is illustrated in the insets, for an incident light angle of  $23.8^\circ$ . The spectral width of the measured gap is indicated by the blue regions. Two peaks whose frequencies correspond with the guided modes of the system appear inside the gap in the spectrum of the waveguide (top). (c) Calculated dispersion relation of the waveguide. The intensity color scale represents the normalized coupling coefficient for the MB perturbation. The horizontal and vertical dotted lines indicate the mechanical band edges and phononic wave vector, respectively, while the black dots represent the frequencies of peaks 1 and 2, all for the top waveguide spectrum shown in (b). The insets in (c) display the mode profiles for the indicated bands where the color represents the normalized out-of-plane displacement.

calculated dispersion relation exhibits nine guided modes but only two (indicated with associated mode profiles) have sufficient mechanical out-of-plane displacement to potentially be detected in experiment. The horizontal dashed lines highlight the edges of the band gap measured in Fig. 3(b) and the black dots correspond to the frequencies of the guided modes measured at different angles. The angle  $\theta = 23.8^\circ$  corresponds to a normalized wavevector of 1.34 (replacing  $q_{\parallel} = n\pi/a$  in Eq. 1 and solving  $n$ ), or  $k_x/(\pi/a) = 0.66$  over the first periodic zone of the waveguide. The two black dots (1 and 2) coincide with the measured frequencies and wavevector in Fig. 3(b). We assume that measured peaks around 7 GHz corresponds with the darker flat mode around 7.7 GHz and not with the lighter curve that it is spectrally closer to. There is a difference of approximately 700 MHz for this band while the other peaks agree very closely with the calculated band. The detection of these two modes is a clear fingerprint of the existence of localized modes along the Shamrock waveguide.

In summary, we provide direct experimental evidence of the complete absence of mechanical vibrations at room temperature within a full phononic band gap that is 5.3 GHz wide with a central frequency of 8.4 GHz, measured using Brillouin light scattering. This measured mechanical gap is significantly wider than previous demonstrations in literature, especially at this frequency regime. Our approach incorporates a geometrical pat-

tern that distributes the mass within the unit cell, forming mass clusters connected by narrow necks that result in the destructive interference of phonon waves, giving rise to these wide mechanical gaps. We achieve control over the width and frequency of the gap by fine-tuning of the geometrical parameters of the structure, enabling spectral tunability of the gap from 4 GHz to 12 GHz. This tunability is extended to the guided modes of a line-defect waveguide, enabling engineering of the frequency and number of localized modes within the structure. This is the first demonstration of mechanical guided modes at hypersonic frequencies in the GHz regime using line-defect waveguides, measured at room temperature without any external excitation. The structures are fabricated on the standard SOI platform which enables facile integration into existing photonic systems. The hypersonic insulator presented here also is a photonic insulator for Transverse-Electric (TE) modes at telecom wavelengths [24, 25] and can be used to simultaneously engineer phononic and photonic transport enhancing the optomechanical coupling between THz photons and GHz phonons. This makes the crystal an ideal transducer in photonic circuits with potential applications in high-speed signal processing [37]. Furthermore, this platform can be used in applications and physical processes in which a wide mechanical band gap is required to isolate the system from thermal damping, such as in quantum cavity optomechanics or organic molecular systems [38].

- [2] J. Chaste et al. A nanomechanical mass sensor with yocotogram resolution. *Nat. Nanotechnol.* **7**, 301 (2012).
- [3] E. Gavartin, P. Verlot and T. J. Kippenberg. A hybrid on-chip optomechanical transducer for ultrasensitive force measurements. *Nat. Nanotechnol.* **7**, 509 (2012).
- [4] J. D. Teufel et al. Sideband cooling of micromechanical motion to the quantum ground state. *Nature* **475**, 359 (2011).
- [5] J. Chan et al. Laser cooling of a nanomechanical oscillator into its quantum ground state. *Nature* **478**, 89 (2011).
- [6] M. Sigalas and E. N. Economou. Band structure of elastic waves in two dimensional systems. *Solid State Commun.* **86**, 141 (1993).
- [7] M. S. Kushwaha, P. Halevi, L. Dobrzynski, and B. Djafari-Rouhani. Acoustic band structure of periodic elastic composites. *Phys. Rev. Lett.* **71**, 2022 (1993).
- [8] R. Martínez-Sala et al. Sound attenuation by sculpture. *Nature* **378**, 241 (1995).
- [9] T. Gorishnyy, C. K. Ullal, M. Maldovan, G. Fytas, and E. L. Thomas. Hypersonic Phononic Crystals. *Phys. Rev. Lett.* **94**, 115501 (2005).
- [10] N. Zen, T. A. Puurtinen, T. J. Isotalo, S. Chaudhuri and I. J. Maasilta. Engineering thermal conductance using a two-dimensional phononic crystal. *Nat. Commun.* **5**, 3435 (2014).
- [11] M. Eichenfield, J. Chan, R. M. Camacho, K. J. Vahala and O. Painter. Optomechanical crystals. *Nature* **462**, 78 (2009).
- [12] B. Djafari-Rouhani, S. El-Jallal and Y. Pennec. Phoxonic crystals and cavity optomechanics. *C. R. Phys.* **17**, 555 (2016).
- [13] G. S. MacCabe et al. Nano-acoustic resonator with ultralong phonon lifetime. *Science* **370**, 840 (2020).
- [14] K. Fang, M. H. Matheny, X. Luan and O. Painter. Optical transduction and routing of microwave phonons in cavity-optomechanical circuits. *Nat. Photon.* **10**, 489 (2016).
- [15] R. N. Patel et al. Single mode phononic wire. *Phys. Rev. Lett.* **121**, 040501 (2018).
- [16] H. Ren et al. Two-dimensional optomechanical crystal cavity with high quantum cooperativity. *Nat. Commun.* **11**, 3373 (2020).
- [17] J. Gomis-Bresco et al. A one-dimensional optomechanical crystal with a complete phononic band gap. *Nat. Commun.* **5**, 4452 (2014).
- [18] S. Mohammadi, A. A. Eftekhar, A. Khelif, W. D. Hunt and Ali Adibi. Evidence of large high frequency complete phononic band gaps in silicon phononic crystal plates. *Appl. Phys. Lett.* **92**, 221905 (2008).
- [19] Y. M. Soliman et al. Phononic crystals operating in the gigahertz range with extremely wide band gaps. *Appl. Phys. Lett.* **97**, 193502 (2010).
- [20] M. Gorisse et al. Observation of band gaps in the gigahertz range and deaf bands in a hypersonic aluminum nitride phononic crystal slab. *Appl. Phys. Lett.* **98**, 234103 (2011).
- [21] W. Cheng, J. Wang, U. Jonas, G. Fytas and N. Stefanou. Observation and tuning of hypersonic bandgaps in colloidal crystals. *Nat. Mater.* **5**, 830 (2006).
- [22] B. Graczykowski et al. Phonon dispersion in hypersonic two-dimensional phononic crystal membranes. *Phys. Rev. B* **91**, 075414 (2015).
- [23] Q. Liu, H. Li and M. Li. Electromechanical Brillouin scattering in integrated optomechanical waveguides. *Optica* **6**, 778 (2019).
- [24] I. Söllner, L. Midolo, and P. Lodahl. Deterministic Single-Phonon Source Triggered by a Single Photon. *Phys. Rev. Lett.* **116**, 234301 (2016).
- [25] G. Arregui, D. Navarro-Urrios, N. Kehagias, C. M. Sotomayor Torres, and P. D. García. All-optical radio-frequency modulation of Anderson-localized modes. *Phys. Rev. B* **98**, 180202(R) (2018).
- [26] COSMOL Inc. COMSOL Multiphysics 5.1 <http://www.comsol.com/> (2022).
- [27] A. H. Safavi-Naeini and O. Painter. Design of optomechanical cavities and waveguides on a simultaneous bandgap phononic-photonic crystal slab. *Opt. Express* **18**, 14926 (2010).
- [28] F. Kargar and A. A. Balandin. Advances in Brillouin-Mandelstam light-scattering spectroscopy. *Nat. Photon.* **15**, 720 (2021).
- [29] G. Carlotti. Elastic Characterization of Transparent and Opaque Films, Multilayers and Acoustic Resonators by Surface Brillouin Scattering: A Review. *Appl. Sciences* **8**, 124 (2018).
- [30] R. W. Boyd, *Nonlinear Optics* 3rd edn. (Academic Press, 2008).
- [31] S. G. Johnson et al. Perturbation theory for Maxwell's equations with shifting material boundaries. *Phys. Rev. E.* **65**, 066611 (2002).
- [32] R. Van Laer, B. Kuyken, D. Van Thourhout and R. Baets. Interaction between light and highly confined hypersound in a silicon photonic nanowire. *Nat. Photon.* **9**, 199 (2015).
- [33] O. Florez et al. Brillouin scattering self-cancellation. *Nat. Commun.* **7**, 11759 (2016).
- [34] J. Cuffe et al. Phonons in Slow Motion: Dispersion Relations in Ultrathin Si Membranes. *Nano Letters* **12**, 3569 (2012).
- [35] L. Brillouin. Diffusion de la lumière et des rayons X par un corps transparent homogène. *Ann. Phys.* **9**, 17. (1922).
- [36] R. Loudon and J. R. Sandercock. Analysis of the light-scattering cross section for surface ripples on solids. *J. Phys. C: solid State Phys.* **13**, 2609 (1980).
- [37] H. Shin et al. Control of coherent information via on-chip photonic-phononic emitter-receivers. *Nat. Commun.* **6**, 6427 (2015).
- [38] B. Gurlek, V. Sandoghdar, D. Martin-Cano. Engineering long-lived vibrational states for an organic molecule. *Phys. Rev. Lett.* **127**, 123603 (2021).

### Acknowledgements

This project has received funding from the European Union's H2020 FET Proactive project TOCHA (No. 824140) and Horizon 2020 research and innovation programme under the Marie Skłodowska-Curie grant agreement No. 754558. The ICN2 authors acknowledge funding by the Severo Ochoa program from Spanish MINECO (No. SEV-2019-0706), Plan Nacional RTI2018-093921-A-C44 (SMOOTH), and MCIN project SIP (PGC2018-101743-B-100), as well as by the CERCA Programme Generalitat de Catalunya. O.F. and G.A. are supported by BIST PhD. Fellowships, R.C.N. by a Marie Skłodowska-Curie fellowship (No. 897148), and P.D.G. by a Ramon y Cajal fellowship No. RyC-2015-18124. M.A. and S.S. gratefully acknowledge funding from the Villum Foundation Young Investigator Program (No. 13170), the Danish National Research Foundation (No. DNRF147 - NanoPhoton), Innovation Fund Denmark (No. 0175-00022 - NEXUS), and Independent Research Fund Denmark (Grant No. 0135-00315 - VAFL).

### Author contributions

O.F. designed, simulated, and characterized the samples. M.A. and S.S. fabricated the samples. G.A., R.C.N., and J.G.B. contributed to the data analysis. C.M.S.T. and P.D.G. supervised the work. P.D.G. conceived the idea and the project. O.F. and P.D.G. wrote the manuscript with contributions and input from all authors.

### Competing financial interests

The authors declare no competing financial interests.

### Methods

Methods are available in the supplementary information.

### Data availability

Data is available upon reasonable request.

## Supplementary Files

This is a list of supplementary files associated with this preprint. Click to download.

- [SupplementaryinformationforEngineeringnanoscalehypersonicphonontransport.pdf](#)